



# Control of localization and optical properties with deep-subwavelength engineered disorder

SEUNGHWA OH,<sup>1</sup> JUNGMIN KIM,<sup>1</sup> XIANJI PIAO,<sup>1</sup> SEULONG KIM,<sup>2</sup> KIHONG KIM,<sup>2</sup> SUNKYU YU,<sup>3</sup> AND NAMKYOO PARK<sup>1,\*</sup>

<sup>1</sup>Photonic Systems Laboratory, Dept. of Electrical and Computer Engineering, Seoul National University, Seoul 08826, Republic of Korea

<sup>2</sup>Department of Physics, Ajou University, Suwon 16499, Republic of Korea

<sup>3</sup>Intelligent Wave Systems Laboratory, Department of Electrical and Computer Engineering, Seoul National University, Seoul 08826, Republic of Korea

\*nkpark@snu.ac.kr

**Abstract:** The effect of deep subwavelength disorder in one-dimensional dichromic multilayer films on the optical transmission, localization length, and Goos–Hänchen shift around the critical angle is analyzed using sets of disordered multilayer films with different degrees of order metric  $\tau$ . For each Gaussian-perturbed multilayer film designed by a Metropolis algorithm targeting the predetermined order metric  $\tau$ , the numerically obtained localization length and transmission show excellent agreement with the recent theoretical analysis developed for disordered multilayer films, further revealing  $\tau$ -dependence of the Goos–Hänchen shift across the critical angle. Emphasizing the role of deep subwavelength structures in disorder-induced transmission enhancement, our result thus paves the way toward the inverse design of a deep subwavelength disordered structural landscape for the targeted order metric  $\tau$  or abnormal optical responses - including the Goos–Hänchen shift.

© 2022 Optica Publishing Group under the terms of the [Optica Open Access Publishing Agreement](#)

## 1. Introduction

The characteristic length of a disordered material is one of the critical parameters for interpreting disorder-induced wave phenomena, as demonstrated in the conditions of branched flows [1] and the transition between transport and localization [2,3]. In the emerging field bridging nanophotonics and disordered photonics, the recent research focus has therefore been directed toward the study of wave localization and diffusion in subwavelength structures [4,5] and investigations of the controlled correlation length for wave transport in disordered media [1]. These efforts have produced unconventional wave behaviors distinct from diffusive transport [6] and weak [7] or strong [8] localization - such as the branched flow of light [1], supporting longer correlation lengths than the wavelength of light. The developments in hyperuniformity [9–13] have clarified the role of structural correlation in reciprocal space, achieving isotropic photonic bandgaps [14–16] and almost perfect transparency [17].

Significant efforts have been made to study *controlled* disorder and correlation length; wave-disorder interactions in perturbed periodic systems [18,19] have been investigated, and controllable subwavelength interactions and unconventional optical properties by means of engineered disorder have been targeted. As summarized in a recent review article [20], the proper manipulation of structural correlation enables the handling of multiple physical quantities, such as spectral responses, transport and localization, angular responses, and topological properties. Though currently incomplete, the quest to reveal the hidden relations between the disorder metrics, characteristic lengths, and various wave properties constitutes the essential core in the understanding and application of disordered systems.

On the other hand, with recent achievements in *deep* subwavelength disorder (DSD) [4,5], it has become sensible to consider the inverse engineering of DSD. For this purpose, considering

the peculiarities in the extreme regime of DSD, such as the breakdown of effective medium theory (EMT) and the associated emergence of the strong localization induced by the accumulated Goos–Hänchen phase shifts [4], there exists a need to reveal the unconventional phenomena of modal localization around the critical angle in relation to the spatial disorder. For example, the abnormal optical responses above the critical angle for noncrystalline “order” with their specific long-range correlations have been studied [21,22] in relation to angle-selective filtering and stronger energy concentration. However, a deeper understanding of the connection between the underlying physical phenomena of the Goos–Hänchen (GH) effect, the spatial order metric, and wave phenomena is still absent, hindering higher-level abstraction or application such as the inverse design DSD structure with the target designer interactions.

In this paper, we inversely design one-dimensional (1D) DSD multilayer films of target order metric  $\tau$  by using a Metropolis algorithm and then study the correlation between the order metric  $\tau$  (0~1, random to periodic), GH effect, and optical characteristics - including localization, transport, and spectral/angular responses. The transitions of the localization behavior at the critical angle depending on the degrees of disorder show good agreement with the analytical derivation of the localization length using the Lyapunov exponent [23], signifying the applicability of engineering disorder in the deep subwavelength domain. We also show that at different scales of disorder with the same film thickness, the disorder-induced transmission is enhanced with DSD perturbation compared to that of subwavelength disorder perturbation, thus emphasizing the role and the need for DSD structures. The enhancement of the Goos–Hänchen shift (GHS) around the critical angle due to induced disorder is also discussed in terms of disorder-induced localization.

## 2. Platforms and method

### 2.1. Disordered structures and $\tau$ order metric

We consider a 1D random dichromic multilayer film sandwiched between a pair of homogeneous dielectrics with the relative permittivity  $\epsilon_{\text{clad}} = 4$ . The multilayer film in Fig. 1 consists of  $N = 200$  pairs of alternating layers of low ( $\epsilon_L = 1$ ) and high ( $\epsilon_H = 5$ ) relative permittivity with thicknesses of  $d_{L,q}$  and  $d_{H,q}$ , respectively, where  $q$  is the index of the layer ( $1 \leq q \leq N$ ) and  $d_{L,q} = d_{H,q} = 20$  nm for the periodic film. The spatial fill factor  $f$  of  $\epsilon_L$  and  $\epsilon_H$  for the whole film is set to be identical ( $f = 0.5$ ), leading to fixed effective permittivity  $\epsilon_{\text{eff}} = (\epsilon_L + \epsilon_H)/2 = 3$  for both periodic and disordered films. We then examine the optical responses through disordered films, considering transverse electric (TE) polarized plane-wave incidences with the incidence angle  $\theta_{\text{in}}$  and the free-space wavelength  $\lambda_0 = 1$  μm.

To address the degree of order of the suggested platform, we apply the translational order metric  $\tau$  originally introduced by Torquato [24]. Specifically, we employ the discrete-space version of the  $\tau$  metric because our structure is pixelized to two-phase heterogeneous media, as similar to [25]. The order metric  $\tau$  defined in [25] measures the statistical deviation of a given disordered film compared to the uncorrelated disorder with a Poisson distribution. For the derivation of the order metric  $\tau$  in dichromic multilayer films, we calculate the static structure factor  $S(k)$  in reciprocal space [26] by introducing the discretized spatial coordinate  $z_p$  (integer  $p \in [1, P]$ ) with the uniform grid size  $\Delta z$ . The total thickness of the heterogeneous film is fixed at  $L$  ( $L = P\Delta z$ , in the current case,  $L = 8$  μm with  $P = 80,000$  and  $\Delta z = 0.1$  nm), and at each  $z_p$  ( $\Delta z/2 \leq z_p \leq L - \Delta z/2$ ), we define the indicator function  $\sigma(p)$  with a binary output  $\sigma(p) = 0$  for the  $\epsilon_L$  layer and  $\sigma(p) = 1$  for the  $\epsilon_H$  layer (see Fig. 1). The  $\epsilon_H$  layer is considered a particle in the point process of  $S(k)$ . The static structure factor  $S(k)$  is then given by:

$$S(k) = \frac{1}{\sigma_H} \left| \sum_{p=1}^P \sigma(p) e^{ikp} \right|^2, \quad (1)$$

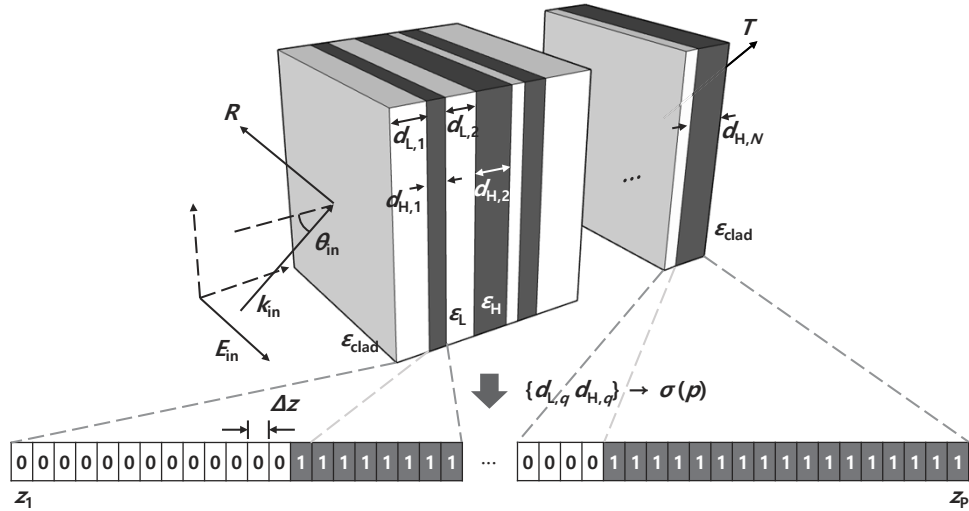


**Fig. 1.** A schematic of a 1D deep-subwavelength disordered multilayer film and the process of converting the thicknesses  $\{d_{L,q}, d_{H,q}\}$  to the indicator function  $\sigma(p)$ . The disordered film consists of layers of varying thicknesses of two alternating materials.  $d_{L,q}$ , and  $d_{H,q}$  denote the thicknesses of the  $\epsilon_L$  layer and  $\epsilon_H$  layer at  $q$ , respectively ( $1 \leq q \leq N$ ). We analyze the effect of disordered profiles on the optical responses (transmittance, characteristic length, and reflection coefficient) to oblique incidence (incidence angle  $\theta_{\text{in}}$ ).  $E_{\text{in}}$  represents the direction of the input electric polarization.

where  $\sigma_H = \sum \sigma(p) = P/2$  is the number of  $\epsilon_H$  sites. The  $\tau$  order metric then becomes

$$\tau = \sum_{k \neq 0} [S(k) - S_p(k)]^2 = \sum_{k \neq 0} [S(k) - (1 - f)]^2, \quad (2)$$

where  $S_p(k) - 1 - f = 0.5$  is the structure factor of the uncorrelated structure obtained from the Poisson point process [10]. As  $\tau$  denotes the deviation from the uncorrelated structure ( $\tau = 0$  with  $S(k) = 0.5$  for all  $k \neq 0$ ), the maximum value of  $\tau = 1$  is that of the periodic film  $\tau_p$ . Normalizing the calculated  $\tau$  of the disordered film to the  $\tau_p$  of the periodic film, we obtain  $\tau \in [0, 1]$ , which we use hereafter.

## 2.2. Inverse design method

To prepare an ensemble of multilayer films achieving the same target order metric  $\tau$  with distinct disordered spatial configurations, we employ the Metropolis algorithm, known to provide an inversely designed canonical ensemble in a stable and straightforward manner [27]. The flowchart for the inverse design process is shown in Fig. 2(a). The initial multilayer film is a periodic film ( $\tau_{\text{initial}} = 1$ ) consisting of  $N$  (200) pairs  $(\epsilon_L, \epsilon_H)$ , with  $d_{L,q} = d_{H,q} = 20$  nm. To achieve a multilayer film with a targeted order metric,  $\tau_{\text{target}}$ , we introduce disorder to the thicknesses of the multilayer film. For the ease of thickness control, we define a thickness matrix  $D$  (and perturbation matrix  $\Delta D$ ) of size  $N \times 2$  with  $d_{L,q}$  and  $d_{H,q}$  as the matrix components at each column representing  $\epsilon_L$  and  $\epsilon_H$  (see Fig. 2(a)). Each column of  $\Delta D$ , i. e.,  $\Delta D_L(\{\Delta d_{L,q}\})$  or  $\Delta D_H(\{\Delta d_{H,q}\})$ , having normal distribution is then generated while keeping  $|\sum \Delta D_L|$  and  $|\sum \Delta D_H| < 0.001$  nm and the number of  $(\epsilon_L, \epsilon_H)$  pairs  $N = 200$  to maintain the total film thickness as well the spatial fill factor  $f = 0.5$ . It is noted that while the continuous perturbation of the thickness could affect the domain size of the simulation space, we suppress its effect on the  $\tau$  order metric by imposing the restriction of  $|\sum \Delta D_{L,H}| < 0.001$  nm in the inverse design process. Therefore, our work can be considered the

inclusion of  $\varepsilon_H$  particles inside the  $\varepsilon_L$  domain (or vice versa), preserving the simulation space, or equivalently the total film thickness.

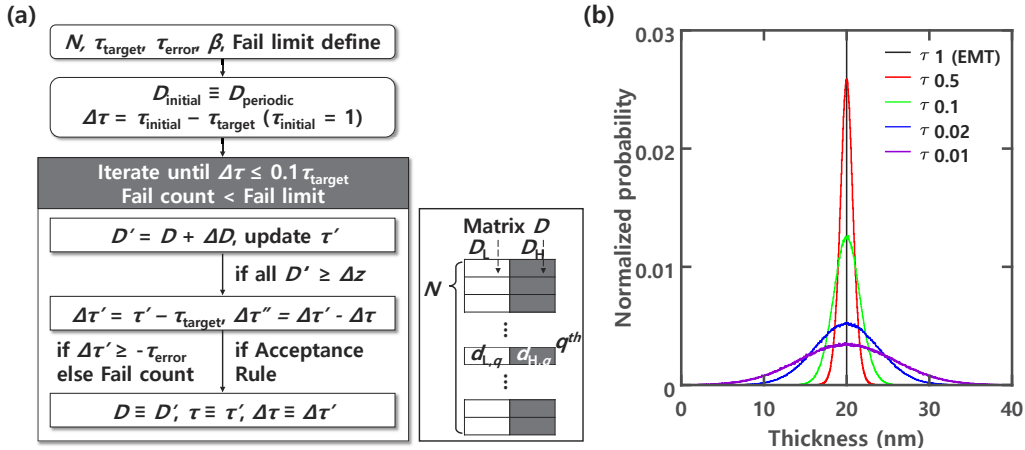


**Fig. 2.** Inverse design process and thickness distributions of multilayer films with  $\tau_{\text{target}}$ . (a) A flowchart of the entire disorder engineering process is illustrated, including the iterative steps of creating and adding the thickness variation  $\Delta D$  to the initial thickness  $D_{\text{periodic}}$  toward the  $D_{\text{final}}$  of  $\tau_{\text{target}}$ . (b) The normalized probability distribution of the film thickness in the ensemble of the identical  $\tau_{\text{target}}$ . As  $\tau_{\text{target}}$  decreases from 0.5 to 0.01, the thickness variation increases as the film structure tends toward more disordered systems.

After  $\sigma(p)$  and  $\tau$  are updated with  $D' = D + \Delta D$ , the deviation of  $\tau$  to  $\tau_{\text{target}}$  ( $\Delta\tau = \tau - \tau_{\text{target}}$ ) is calculated, and the process is repeated until  $\Delta\tau < 0.1\tau_{\text{target}}$ . The final output of the Metropolis algorithm then becomes  $D_{\text{final}}$  for the disordered multilayer film of  $\tau_{\text{target}}$ , with 200 pairs of layer thicknesses  $d_{L,q}$ , and  $d_{H,q}$ . Care must be taken to optimize the distribution of  $\Delta D$  because a variation that is too large leads to a penalty in precision. The standard deviation of  $\Delta D_L$  or  $\Delta D_H$  is set to be  $\Delta\tau$  dependent, 0.25 nm when  $|\Delta\tau| < 0.05$  and 0.5 nm otherwise, to optimize both the computation time and precision. The success rate of multilayer film generation for a given  $\tau_{\text{target}}$  was over 83% out of 3,000 realizations, confirming the stability of the inverse design process. The obtained relationship between  $\tau_{\text{target}}$  and the distribution of the multilayer film thicknesses is shown in Fig. 2(b). As  $\tau_{\text{target}}$  decreases, the thickness distribution disperses as expected ( $\tau_{\text{target}} = 0.5, 0.1, 0.02$ , and  $0.01$ ). The variation in the critical angle using the effective permittivity  $\theta_c = \arcsin((\varepsilon_{\text{eff}}/\varepsilon_{\text{clad}})^{1/2})$ , where  $\varepsilon_{\text{eff}} = (\varepsilon_L + \varepsilon_H)/2 = 3$ , is within  $3 \times 10^{-4}$  degrees for all realizations, confirming that all realizations are equal in the EMT sense. It is worth to note that our design approach of applying the normal-distribution perturbation to the layer thickness corresponds to the systematic perturbation of lattice structures, leading to Gaussian-perturbed lattices. In view of a much larger space of material phases offered by disorder, our method thus covers a specific subspace in the material phase: including both short-range and long-range density fluctuations while preserving a significant amount of long-range periodic order [28]. While the variety of material phases is assured in our implementation guaranteed by the target order metric  $\tau$  between 0 (Random) and 1 (Periodic), the extension of the study for different material phase spaces would be possible, for example, by varying the probability density function in the perturbation which is currently the normal distribution, or utilizing other models that provides highly correlated yet disordered landscape without Bragg peaks.

### 3. Engineered DSD film for optical response control around the critical angle

For 1D DSD structures near the critical angle  $\theta_c$ , there exists an abnormality [29] deviating from the EMT due to the differences in a phase accumulation arising from DSD. When the thickness variation of the layers is on a deep subwavelength scale, in addition to the phase accumulation from the propagation delay, the phase accumulation through Fresnel reflection, a.k.a. the Goos–Hänchen phase shift, starts to contribute. Sheinfux [4] studied the case of a 1D film with *uncorrelated* disorder focusing on the abnormal transmission around  $\theta_c$ , identifying two different regimes of TE incident angle according to the wave behavior inside the layers. The two characteristic critical angles are given by  $\theta_L = \arcsin((\varepsilon_L/\varepsilon_{clad})^{1/2})$  and  $\theta_c = \arcsin((\varepsilon_{eff}/\varepsilon_{clad})^{1/2})$  for the permittivity of the cladding material  $\varepsilon_{clad}$ . The regime of  $\theta_L < \theta < \theta_c$  is called the Goos–Hänchen *localization* (GHL) regime, as the translation phase accumulation achieved by Fresnel reflection induces localization in this regime. The regime of  $\theta_c < \theta$  is defined as the effective medium *evanescence* (EME) regime, as the overall transmittance decays exponentially. In this regime, a narrower-bandwidth localization with a higher quality factor  $Q$  also appears, which is the main reason for the “abnormal” narrowband transmission enhancement in the EME regime, where the exponential decay of the transmission is natural.

Considering that this abnormal transmission in the EME regime is attributed to the overwhelming localization in the subwavelength disordered structure [4], improving the abnormal transmission in the EME regime should be possible by proactively engineering the degree of disorder. Here, we employ the  $\tau$  order metric, which is used as a control parameter in the ensemble of disordered films, where “order” means a crystal with long-range order with salient Bragg peaks and “random” refers to an uncorrelated, fully random disordered distribution. For the inversely designed DSD film ensembles, 3,000 realizations of each  $\tau_{target}$  using the Metropolis algorithm and the optical responses (transmission and reflection at incident angles between  $0^\circ$  and  $66^\circ$ ) were analyzed using the transfer matrix method (TMM). Most importantly, we numerically calculated the wave-localization length at each  $\tau_{target}$  with  $\xi^{-1} = -\langle \ln T \rangle / L$  [30] by taking the ensemble average over the group of realizations at a given  $\tau_{target}$ , where  $T$  is the transmission of each realization and  $L$  is the thickness of the multilayer film. For comparison with the numerical result, the analytical calculation of the localization length  $\xi$  was carried out assuming the same permittivity realization following the procedures in [23]. This has not been tested for DSD structures or the Goos–Hänchen phase shift for its validity.

In detail, the disordered multilayer films in [23] are assumed to be an inhomogeneous slab of  $\varepsilon(z) = \varepsilon_{eff} + \delta\varepsilon(z)$ , where  $\varepsilon_{eff} = \langle \varepsilon(z) \rangle$  and  $\langle \delta\varepsilon(z) \rangle = 0$  ( $0 \leq z \leq L$ ). With a cladding of  $\varepsilon_{clad}$  and an obliquely impinging s-polarized plane wave where  $k^2 = \varepsilon_E k_0^2$ , the complex amplitude of the electric field  $E$  inside the media becomes

$$\frac{\partial^2 E}{\partial z^2} + [k_0^2 \varepsilon(z) - k^2 \sin^2 \theta_{in}] E = \frac{\partial^2 E}{\partial z^2} + (k \cos \theta_{in})^2 \left[ 1 + \frac{\varepsilon_{eff}/\varepsilon_{clad} - 1 + \delta\varepsilon(z)/\varepsilon_{clad}}{\cos^2 \theta_{in}} \right] E = 0. \quad (3)$$

For the random distribution of the present permittivity profile, we adopt a short-range correlation model in [31] with the correlation length  $l_c$

$$\langle \delta\varepsilon(z) \delta\varepsilon(z') \rangle = \rho^2 \exp(-|z - z'|/l_c), \quad \langle \delta\varepsilon(z) \rangle = 0, \quad (4)$$

where a random variable  $\delta\varepsilon(z) = \delta\varepsilon(z)/\varepsilon_{clad}$ , which is further reduced to

$$\langle \delta\varepsilon(z) \delta\varepsilon(z') \rangle = 2g_0 \delta(z - z'), \quad \langle \delta\varepsilon(z) \rangle = 0, \quad (5)$$

in the case of  $\rho \rightarrow \infty$ ,  $l_c \rightarrow 0$  and  $\rho^2 l_c \rightarrow g_0$ , where  $g_0$  is the strength of disorder. The analytic expression of the localization length  $\xi$  can be written as

$$\frac{1}{\xi} = 2k(kg_0)^{1/3} F \left( \frac{\sin^2 \theta_{in} - \epsilon_{eff}/\epsilon_{clad}}{(kg_0)^{2/3}} \right), \quad (6)$$

where  $F(X)$  is expressed in the Airy functions and their derivatives

$$F(X) = \frac{Ai(X)Ai'(X) + Bi(X)Bi'(X)}{[Ai(X)]^2 + [Bi(X)]^2}. \quad (7)$$

The localization length  $\xi$  and the ensemble-averaged transmission  $\langle \ln T \rangle$  of various  $\tau_{target}$  values of realizations ( $\tau_{target} = 0.5, 0.1, 0.02, 0.01$ , and  $\tau = 1$ , periodic multilayer film or EMT homogeneous film) are plotted as a function of the incident angle  $\theta$  (Fig. 3). The conventional abrupt transition of localization length  $\xi(\theta)$  and average transmission across the  $\theta_c$  of the homogeneous film (thick solid black line) is clear, as the wave transmission through the film across  $\theta_c$  changes from Fabry-Pérot resonance to total internal reflection and the accompanying evanescent decay. In contrast, when disorder increases ( $\tau_{target}$  changes from 1 to 0), the transition of the localization length  $\xi(\theta)$  (Fig. 3(a)) and average transmission  $\langle \ln T(\theta) \rangle$  (Fig. 3(b)) across  $\theta_c$  tend to depart from those of the EMT case. The transition across  $\theta_c$  becomes smoother due to the disorder-induced high- $Q$  localization and higher transmission in the  $\theta_{in} > \theta_c$  regime (see Fig. 3(c)). It is noted that the analytically obtained  $\xi(\theta)$  and  $\langle \ln T(\theta) \rangle$  from Eq. (6) (square markers) present good agreement with the numerically obtained results, with the fitting parameter of the disorder strength  $g_0$  (0.029 nm for  $\tau = 0.5$ , 0.035 nm for  $\tau = 0.1$ , 0.102 nm for  $\tau = 0.02$ , and 0.213 nm for  $\tau = 0.01$ ). For even lower  $\tau_{target} < 0.01$ , abnormal transmission at even larger  $\theta_{in}$  is possible.

The result in Fig. 3 thus reveals the correlations between the degree of disorder and the abnormal transmission, as well as the characteristic length. Most importantly, this result also demonstrates the localization control across  $\theta_c$  based on the target order metric  $\tau_{target}$ . Considering that the disorder-induced abnormal transmission has narrowband peaks above  $\theta_c$  (see Fig. 3(c)), a proper choice of  $\tau_{target}$  realization can be used to derive unique optical applications such as a sensitive angular filter.

Revealing the effect of the order metric  $\tau$  on the optical properties around  $\theta_c$ , we further examine the effect of the *scale of disorder* to determine whether it is desirable to increase the number of disordered deep-subwavelength layers at the same multilayer film thickness. For this, we start from the films used in the previous section and then generate a new set of films composed of disordered layers of average permittivity within the effective layer thickness  $\Lambda$ . In Fig. 4, we plot the average transmission  $\langle \ln T(\theta) \rangle$  across  $\theta_c$  for the new sets of films; the realizations originally have  $\tau = 0.5$  and 0.01, with  $\Lambda = 40$  nm to 1000 nm. As  $\Lambda$  increases, the average transmission  $\langle \ln T(\theta) \rangle$  approaches that of the EMT result, as expected. Most interestingly, the deviation from the EMT scenario, or the emergence of abnormal transmission, is more pronounced for the films derived from highly disordered seed films ( $\tau = 0.01$ ) and for smaller  $\Lambda$ . This result implies and confirms the role and the need for DSD structures to control abnormal optical properties around  $\theta_c$ .

Considering the above result, DSD modulates localization within the film; its effect on the GHS around the critical angle is worth investigating. The GHS is a lateral displacement of the reflected finite-cross-section beam relative to the ideal plane wave reflection at the point of incidence. The GHS has been mainly discussed in the total internal reflection condition  $\theta_{in} > \theta_c$ , focusing on its shift length or frequency tunability. While the tuning of the GHS is achieved by using the resonance at a dielectric/dielectric or metal/dielectric interface [32–36] and by introducing defect states within the structure [37], the DSD multilayer film in this paper

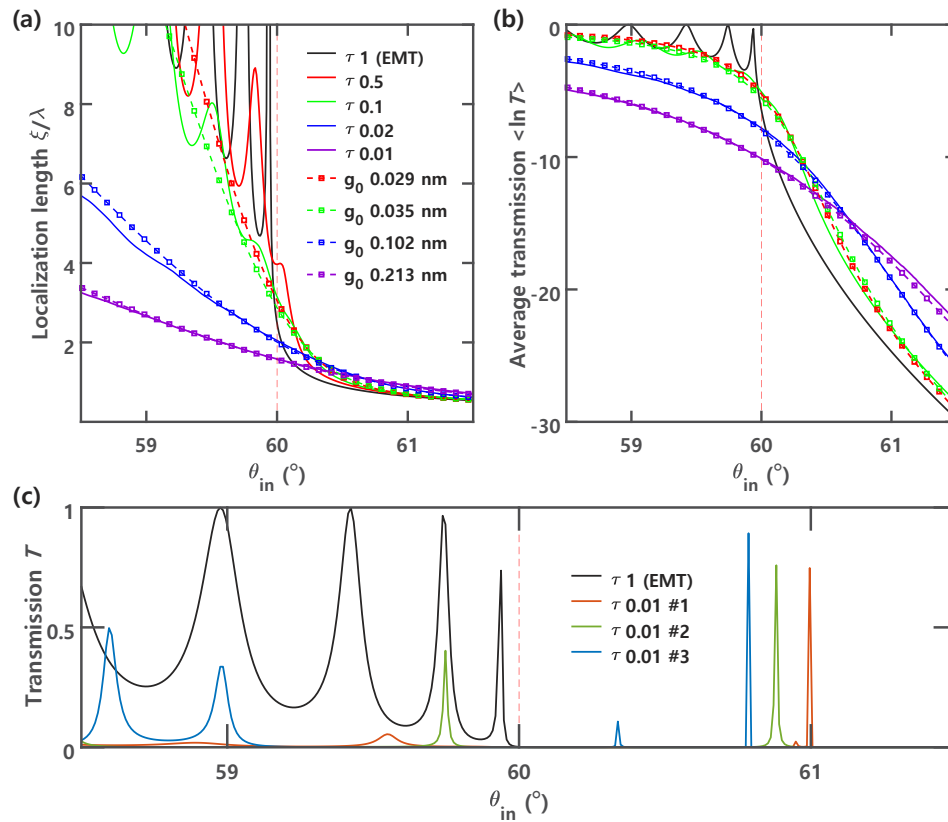


**Fig. 3.** The localization length and the average transmission for the  $\tau_{\text{target}}$  DSD film ensembles. (a) The localization length  $\xi$  is calculated from the transmission obtained with TMM. The thick solid black line indicates the localization length of the bulk EMT film. The localization length is in units of  $\lambda$ , the wavelength in the surrounding medium. (b) The colored lines are the ensemble-averaged transmission  $\langle \ln T \rangle$ , and the square markers represent the analytically obtained localization length with fitting parameter  $g_0$  from 0.03 to 0.2 nm. (c) Three disordered realizations, with  $\tau_{\text{target}} = 0.01$ , exhibit abnormal transmission peaks above  $\theta_c$ .

as a generalized defect system could provide an additional platform for GHS engineering. To quantitatively study the correlation between the GHS and disorder metric  $\tau$ , we introduce the metric of the GHS,  $D_s$ , which is calculated by using the phase of the reflection coefficient; first derived by Artmann using the stationary phase method [38],

$$D_s = -\frac{\lambda}{2\pi} \frac{d\varphi(\theta_{in})}{d\theta_{in}}, \quad (8)$$

where  $\varphi(\theta_{in})$  is the phase of the reflection coefficient at  $\theta_{in}$ . The calculated wavelength-normalized average GHS,  $\langle D_s \rangle$ , is plotted for various  $\tau$  values in Fig. 5(a), taking the average from each group of  $\tau_{\text{target}}$  realizations. The obtained  $\langle D_s \rangle$  ranges from  $0 \sim 10 \mu\text{m}$  ( $0 \sim 20 \lambda$ ) at  $\theta_{in} \sim 61^{\circ}$  ( $> \theta_c$ ), as the wavelength in the cladding medium is 500 nm. It is noted that near or below  $\theta_c$ ,  $\langle D_s \rangle$  gets large for larger  $\tau$ . However, above  $\theta_c$ , where the disorder-induced abnormal transmission prevails,  $\langle D_s \rangle$  dramatically increases for lower  $\tau$ , i.e., for highly disordered realizations. This result demonstrates that the localization induced by DSD can be used for GHS engineering by tailoring  $\tau_{\text{target}}$ , in addition to the conventional resonance control [33–36].

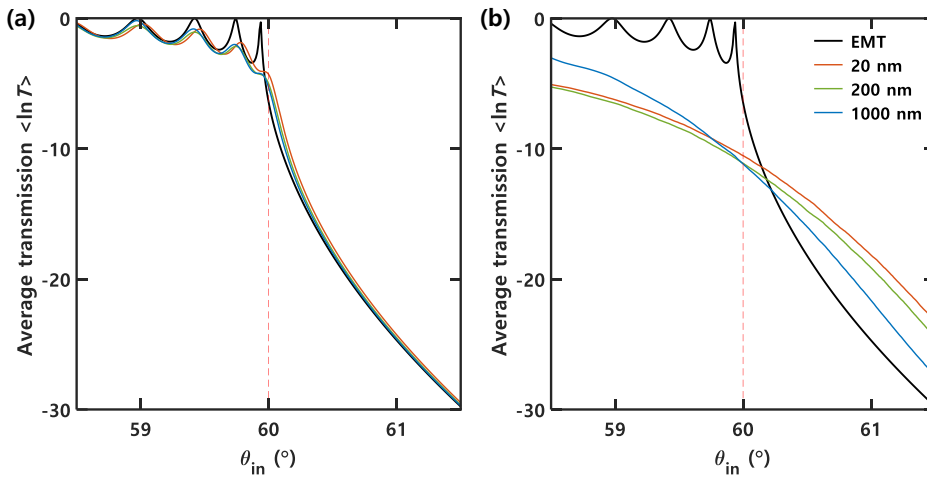


**Fig. 4.** Calculated average transmission  $\langle \ln T(\theta) \rangle$  with various effective layer thicknesses,  $\Lambda$ . The new sets of films, generated using the average permittivity with  $\Lambda$ , are used for the calculation. The original sets of realizations have (a)  $\tau = 0.5$  and (b)  $\tau = 0.01$ . The colored lines represent the average transmission of  $\Lambda = 20$  nm, 200 nm, and 1000 nm. The disorder-induced abnormal transmission across  $\theta_c$  varies in response to  $\Lambda$ .  $\langle \ln T(\theta) \rangle$  approaches EMT (thick solid black line) as  $\Lambda$  increases. For smaller  $\Lambda$ , the emergence of abnormal transmission (deviation from the EMT) is more pronounced, implying the role of DSD structures in controlling abnormal optical properties around  $\theta_c$ .

To provide better insight into the effect of DSD on the GHS, we used the finite element method (COMSOL Multiphysics) to determine the intensity of the electric field reflected from multilayer films with different DSD landscapes. An incident beam at  $60.16^\circ$ , above  $\theta_c$ , with a spatial Gaussian profile width of  $4\lambda$  was considered using plane wave expansion. The periodic multilayer film of  $\tau = 1$  and the DSD multilayer film of  $\tau = 0.01$  (#1 in Fig. 3(c)) were compared. For both cases, the confinement of the field at the film boundary and the conventional GHS were observed (blue arrows in Fig. 5(b) and Fig. 5(c)) to have a lateral shift of  $7.6\lambda$ , which is in good agreement with Fig. 5(a). We note that both films exhibiting the same magnitude of GHS at different  $\tau$  values implies the signature of EMT approximation on the wavelength scale.

However, in contrast to Fig. 5(b), an auxiliary GHS was observed for the highly disordered film (Fig. 5(c)). With the strong localization within the DSD structure, the trapped field propagates along the  $x$ -direction and creates an auxiliary GHS of  $86.4\lambda$ , coupling with the cladding material (red arrow in Fig. 5(c)). It is emphasized that the field strength and the evolution of the auxiliary GHS beam in the DSD film are in line with the variation in average permittivity (overlapping yellow lines in Fig. 5(c)), thus providing an additional degree of freedom for GHS engineering utilizing disorder, unlike conventional GHS tuning based on surface resonance control. The auxiliary GHS in a disordered structure is also observable in transverse magnetic (TM) polarized incident waves. The calculated  $\langle D_s \rangle$  in TM polarization is plotted for various  $\tau$  values in Fig. 5(d), taking the average from each group of  $\tau_{\text{target}}$  realizations. In Fig. 5(e) and Fig. 5(f), the intensity of the magnetic field of the incidence at  $40.68^\circ$  (above  $\theta_{c-TM}$ , where  $\theta_{c-TM} = \arcsin((\epsilon_{\text{eff-TM}}/\epsilon_{\text{clad}})^{1/2})$  and  $\epsilon_{\text{eff-TM}} = 2\epsilon_L\epsilon_H/(\epsilon_L + \epsilon_H) - 1.67$ ) with a spatial Gaussian profile width of  $4\lambda$  is depicted. The disordered film used in Fig. 5(f) is the same realization as that in Fig. 5(c). As in Fig. 5(b) and Fig. 5(c), both cases have the conventional GHS of  $5.3\lambda$  (blue arrows in Fig. 5(e) and Fig. 5(f)), which is in good agreement with Fig. 5(d), while an auxiliary GHS of  $83.9\lambda$  is also observable in the disordered case (red arrow in Fig. 5(f)).

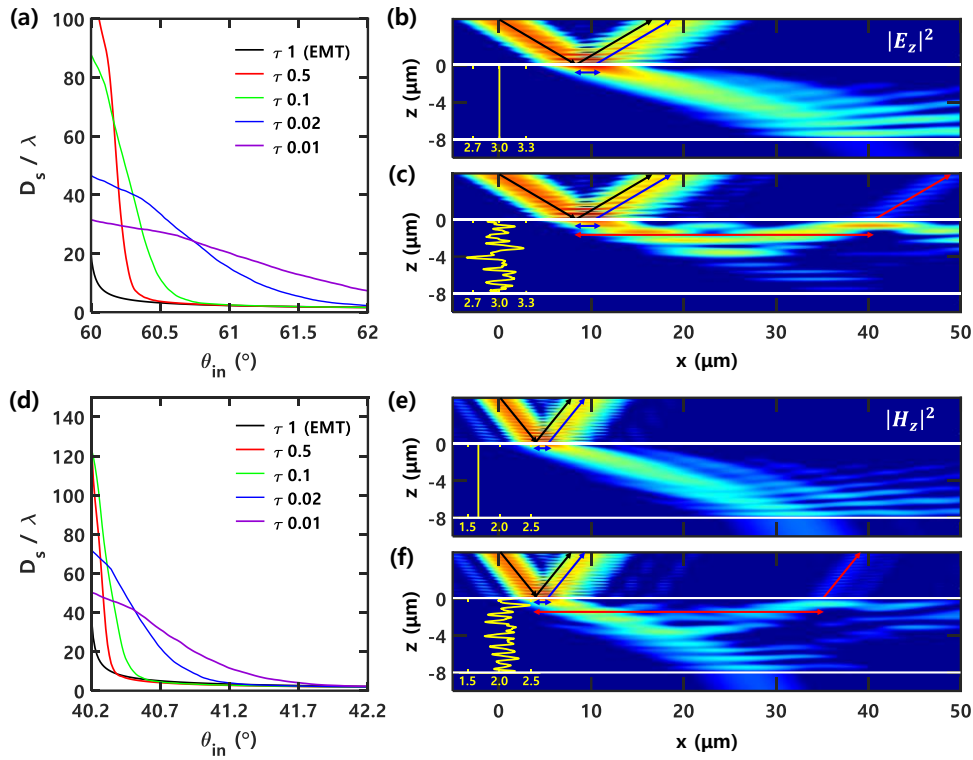


**Fig. 5.** (a) The ensemble-averaged GHS for each group of  $\tau_{\text{target}}$  realizations (TE polarization). The GHS calculation is based on Eq. (8). Above  $\theta_c$ , the GHS becomes larger at low  $\tau$  realizations. The calculated electric field distribution in the (b) periodic and (c) disordered ( $\tau = 0.01 \# 1$ ) films. The conventional GHS (blue arrow) is observed in both cases. In (c), the trapped field and an auxiliary lateral shift (red arrow) are depicted. The emergence of the auxiliary shift originates from the localized field, which is trapped and propagated along the positive  $x$ -direction and results in an 11-fold enhancement from the conventional shift. (d) The ensemble-averaged GHS for each group of  $\tau_{\text{target}}$  realizations (TM polarization). The calculated magnetic field distribution of the TM polarized incidence on (e) periodic and (f) disordered ( $\tau = 0.01 \# 1$ ) films. The conventional GHS (blue arrow) is observed in both cases. In (e), the trapped field and an auxiliary lateral shift (red arrow) are depicted. As in TE polarization, the emergence of the auxiliary shift originates from the localized field and results in a 15-fold enhancement from the conventional shift. The total thicknesses  $L$  of the films are the same, 8  $\mu\text{m}$ . The overlapping yellow lines depict the average permittivity variations through the thickness domain  $z$  on the wavelength scale. The localized field locations within the film match the high permittivity peaks.

#### 4. Conclusion

To conclude, in the deep subwavelength disorder regime, we studied the controllable localization inside of a 1D multilayer film above the critical angle that arises as a result of an interplay between evanescence and disorder. We applied the disorder metric  $\tau$  to define the disorder strength and engineered disordered films with targeted  $\tau$  by inducing thickness variation in units of  $\sim \lambda_0 / 10,000$ . This disorder-induced localization causes abnormal transmission and localization length around the critical angle, and the result is in excellent agreement with the theoretical analysis developed for randomly stratified dielectric media. Considering that the disorder-induced abnormal transmission has narrowband peaks above  $\theta_c$ , the correlation study

between the degree of DSD and the abnormal optical characteristics shows potential for disorder engineering for unique optical applications, such as a sensitive angular filter. We also emphasized the role of the deep subwavelength scale by exhibiting improved transmission enhancement of deep-subwavelength perturbation compared to that of subwavelength scale disturbance. Most importantly, due to the trapped field in the disordered multilayer film caused by disorder-induced localization, an auxiliary lateral shift 11 times larger than the conventional GHS in the periodic multilayer film is observed in TE polarization. This auxiliary GHS is polarization-independent, as a similar enhancement is observed in TM polarization. The fundamental mechanism of the auxiliary GHS and the disorder-induced localization constitute a new perspective for GHS engineering, where disorder has so far been dealt with only in terms of robustness. Our work proposes disorder engineering applications for controlling abnormal optical characteristics around the critical angle  $\theta_c$ . Significantly, the emergence and enhancement of the auxiliary GHS are considered promising in GHS tunability studies. A similar approach with different material phase spaces would be also possible, by modifying and engineering the probability density function in the perturbation.

**Funding.** National Research Foundation of Korea (2014M3A6B3063708, 2021R1C1C1005031).

**Acknowledgments.** We thank the National Research Foundation of Korea for financial support for this work.

**Disclosures.** The authors declare no conflicts of interest.

**Data availability.** Data underlying the results presented in this paper are not publicly available at this time but may be obtained from the authors upon reasonable request.

## References

1. A. Patsyk, U. Sivan, M. Segev, and M. A. Bandres, "Observation of branched flow of light," *Nature* **583**(7814), 60–65 (2020).
2. P. Sheng, *Introduction to Wave Scattering, Localization and Mesoscopic Phenomena* (Springer, 1995).
3. S. Yu, X. Piao, and N. Park, "Disordered Potential Landscapes for Anomalous Delocalization and Superdiffusion of Light," *ACS Photonics* **5**(4), 1499–1505 (2018).
4. H. Herzig Sheinfux, I. Kaminer, A. Z. Genack, and M. Segev, "Interplay between evanescence and disorder in deep subwavelength photonic structures," *Nat. Commun.* **7**(1), 12927 (2016).
5. H. H. Sheinfux, Y. Lumer, G. Ankonina, A. Z. Genack, G. Bartal, and M. Segev, "Observation of Anderson localization in disordered nanophotonic structures," *Science* **356**(6341), 953–956 (2017).
6. P. Barthelemy, J. Bertolotti, and D. S. Wiersma, "A Lévy flight for light," *Nature* **453**(7194), 495–498 (2008).
7. B. L. Altshuler, D. Khmel'nitzkii, A. I. Larkin, and P. A. Lee, "Magnetoresistance and Hall effect in a disordered two-dimensional electron gas," *Phys. Rev. B* **22**(11), 5142–5153 (1980).
8. P. W. Anderson, "Absence of Diffusion in Certain Random Lattices," *Phys. Rev.* **109**(5), 1492–1505 (1958).
9. S. Torquato and F. H. Stillinger, "Local density fluctuations, hyperuniformity, and order metrics," *Phys. Rev. E* **68**(4), 041113 (2003).
10. S. Torquato, "Hyperuniform states of matter," *Phys. Rep.* **745**, 1–95 (2018).
11. J. Kim and S. Torquato, "Characterizing the hyperuniformity of ordered and disordered two-phase media," *Phys. Rev. E* **103**(1), 012123 (2021).
12. D. Chen and S. Torquato, "Designing disordered hyperuniform two-phase materials with novel physical properties," *Acta Mater.* **142**, 152–161 (2018).
13. R. D. Batten, F. H. Stillinger, and S. Torquato, "Classical disordered ground states: Super-ideal gases and stealth and equi-luminous materials," *J. Appl. Phys.* **104**(3), 033504 (2008).
14. M. Florescu, S. Torquato, and P. J. Steinhardt, "Designer disordered materials with large, complete photonic band gaps," *Proc. Natl. Acad. Sci.* **106**(49), 20658–20663 (2009).
15. W. Man, M. Florescu, E. P. Williamson, Y. He, S. R. Hashemizad, B. Y. C. Leung, D. R. Liner, S. Torquato, P. M. Chaikin, and P. J. Steinhardt, "Isotropic band gaps and freeform waveguides observed in hyperuniform disordered photonic solids," *Proc. Natl. Acad. Sci.* **110**(40), 15886–15891 (2013).
16. W. Man, M. Florescu, K. Matsuyama, P. Yadak, G. Nahal, S. Hashemizad, E. Williamson, P. Steinhardt, S. Torquato, and P. Chaikin, "Photonic band gap in isotropic hyperuniform disordered solids with low dielectric contrast," *Opt. Express* **21**(17), 19972–19981 (2013).
17. O. Leseur, R. Pierrat, and R. Carminati, "High-density hyperuniform materials can be transparent," *Optica* **3**(7), 763–767 (2016).
18. L. Martin, G. Di Giuseppe, A. Perez-Leija, R. Keil, F. Dreisow, M. Heinrich, S. Nolte, A. Szameit, A. F. Abouraddy, D. N. Christodoulides, and B. E. A. Saleh, "Anderson localization in optical waveguide arrays with off-diagonal coupling disorder," *Opt. Express* **19**(14), 13636–13646 (2011).

19. A. Ortega-Moñux, J. Čtyroký, P. Cheben, J. H. Schmid, S. Wang, Í. Molina-Fernández, and R. Halir, "Disorder effects in subwavelength grating metamaterial waveguides," *Opt. Express* **25**(11), 12222–12236 (2017).
20. S. Yu, C.-W. Qiu, Y. Chong, S. Torquato, and N. Park, "Engineered disorder in photonics," *Nat. Rev. Mater.* **6**(3), 226–243 (2021).
21. M. Coppolaro, G. Castaldi, and V. Galdi, "Effects of deterministic disorder at deeply subwavelength scales in multilayered dielectric metamaterials," *Opt. Express* **28**(7), 10199–10209 (2020).
22. M. Coppolaro, G. Castaldi, and V. Galdi, "Anomalous light transport induced by deeply subwavelength quasiperiodicity in multilayered dielectric metamaterials," *Phys. Rev. B* **102**(7), 075107 (2020).
23. K. Kim, "Exact localization length for s-polarized electromagnetic waves incident at the critical angle on a randomly-stratified dielectric medium," *Opt. Express* **25**(23), 28752–28763 (2017).
24. S. Torquato, G. Zhang, and F. H. Stillinger, "Ensemble Theory for Stealthy Hyperuniform Disordered Ground States," *Phys. Rev. X* **5**(2), 021020 (2015).
25. R. A. DiStasio, G. Zhang, F. H. Stillinger, and S. Torquato, "Rational design of stealthy hyperuniform two-phase media with tunable order," *Phys. Rev. E* **97**(2), 023311 (2018).
26. E. Chertkov, R. A. DiStasio, G. Zhang, R. Car, and S. Torquato, "Inverse design of disordered stealthy hyperuniform spin chains," *Phys. Rev. B* **93**(6), 064201 (2016).
27. S. Torquato, *Random Heterogeneous Materials: Microstructure and Macroscopic Properties* (Springer, 2002).
28. M. A. Klatt, J. Kim, and S. Torquato, "Cloaking the underlying long-range order of randomly perturbed lattices," *Phys. Rev. E* **101**(3), 032118 (2020).
29. H. Herzog Sheinfux, I. Kaminer, Y. Plotnik, G. Bartal, and M. Segev, "Subwavelength Multilayer Dielectrics: Ultrasensitive Transmission and Breakdown of Effective-Medium Theory," *Phys. Rev. Lett.* **113**(24), 243901 (2014).
30. K. Y. Bliokh and V. D. Freilikher, "Localization of transverse waves in randomly layered media at oblique incidence," *Phys. Rev. B* **70**(24), 245121 (2004).
31. J. W. Kantelhardt, R. Berkovits, S. Havlin, and A. Bunde, "Are the phases in the Anderson model long-range correlated?" *Phys. A* **266**(1-4), 461–464 (1999).
32. J. Wu, F. Wu, K. Lv, Z. Guo, H. Jiang, Y. Sun, Y. Li, and H. Chen, "Giant Goos-Hänchen shift with a high reflectance assisted by interface states in photonic heterostructures," *Phys. Rev. A* **101**(5), 053838 (2020).
33. W. Kong, Y. Sun, and Y. Lu, "Enhanced Goos-Hänchen shift of graphene coated on one-dimensional photonic crystal," *Results Phys.* **17**, 103107 (2020).
34. X. Du and H. Da, "Large and controlled Goos-Hänchen shift in monolayer graphene covered multilayer photonic crystals grating," *Opt. Commun.* **483**, 126606 (2021).
35. D. Zhao, S. Ke, Q. Liu, B. Wang, and P. Lu, "Giant Goos-Hänchen shifts in non-Hermitian dielectric multilayers incorporated with graphene," *Opt. Express* **26**(3), 2817–2828 (2018).
36. Z. Liu, F. Lu, L. Jiang, W. Lin, and Z. Zheng, "Tunable Goos-Hänchen Shift Surface Plasmon Resonance Sensor Based on Graphene-hBN Heterostructure," *Biosensors* **11**(6), 201 (2021).
37. M. Mao, T. Zhang, S. Guo, and H. Zhang, "Goos-Hänchen shift produced by a one-dimensional photonic crystal doped with InSb," *J. Opt. Soc. Am. B* **37**(7), 2095–2103 (2020).
38. K. Artmann, "Berechnung der Seitenversetzung des totalreflektierten Strahles," *Ann. Phys. (Berlin, Ger.)* **437**(1-2), 87–102 (1948).